

Measuring the topological charge of ultrabroadband, optical-vortex beams with a triangular aperture

Matthew E. Anderson,^{1,*} Heath Bigman,¹ Luís E. E. de Araujo,² and Jan L. Chaloupka³

¹Department of Physics, San Diego State University, San Diego, California 92182, USA

²Instituto de Física “Gleb Wataghin,” Universidade Estadual de Campinas, Campinas, Sao Paulo, 13083-859, Brazil

³Department of Physics, University of Northern Colorado, Greeley, Colorado 80639, USA

*Corresponding author: matt@sciences.sdsu.edu

Received February 8, 2012; revised June 13, 2012; accepted June 16, 2012;
posted June 18, 2012 (Doc. ID 162786); published July 16, 2012

A simple technique for determining the topological charge of supercontinuum optical vortices is presented. The spatial dispersion inherent to generating broadband vortices with a single forked grating is compensated with a double-pass arrangement from a single spatial light modulator. The vortex charge is determined by inspecting the diffraction pattern through a triangular aperture. It is shown that the topological charge is constant, and can be consistently measured, across a wide range of colors. © 2012 Optical Society of America

OCIS codes: 050.4865, 050.1950.

1. INTRODUCTION

Optical vortices have garnered much attention in recent years. With the introduction of optical phase singularities by Nye and Berry [1], and the subsequent demonstration that vortex beams can carry orbital angular momentum [2], there has been steady research in the generation of vortex beams from static and programmable optical elements. Several review articles exist, including an excellent discussion by Dennis *et al.* [3]. The production of vortex beams with continuous-wave (cw) lasers has been explored in great detail [4]. Recently, the generation of vortex beams with femtosecond (fs) lasers has also been demonstrated [5]. With their increased bandwidth, fs pulses create a dispersion problem that does not plague vortex generation with cw lasers. Namely, the common approach of using a forked grating to create a vortex in the first-order diffracted beam creates a large amount of spatial chirp with a broad-bandwidth fs laser source. This spatial dispersion may be compensated with the use of a second grating [5–7], or by a second reflection off the same spatial-light modulator (SLM) [8], using the “unused” portion of the initial forked grating pattern. It has been demonstrated that 20 fs vortex beams may be generated using a prism pair and a forked grating [9]. It has also been demonstrated that arbitrary spatial patterns may be generated in fs fields with two SLMs [10]. Vortices generated from the output of a microstructured optical fiber have also attracted attention recently [11]. With the octave-spanning bandwidth available in these supercontinuum (SC) sources, the dispersion problem becomes even more extreme. The theoretical treatment of colored vortices has been studied extensively by Berry [12], and several approaches have been demonstrated for achromatic white-light vortices, including the use of a SLM and prism to explore chromatic effects in a white-light vortex [13], the demonstration of achromatic Bessel beams [14], and the use of an axially symmetric polarizer combined with waveplates and linear polarizers to generate SC vortices [15].

Various techniques have been developed in recent years to measure the orbital angular momentum of optical vortex beams. For instance, the use of a second SLM permits the sorting of angular momentum states and the determination of their charge [16,17] and spectrum [18]. Damann gratings have been used to sort vortex beams [19]. It was also shown that the intensity profile in the focal plane of a cylindrical lens contains information about the charge of polychromatic vortex beams [20]. This simple technique was applied successfully to measure the charge of fs vortex beams [21]. Another approach for measuring vortex charge was recently demonstrated that uses a triangular aperture to diffract the beam [22]. The ensuing diffraction pattern contains information on the magnitude and sign of the topological charge. It was subsequently demonstrated that this technique could be applied to narrowband fs vortex beams and non-integer vortices with a metallic triangular aperture [23]. For fs pulses, this noninterferometric technique is much simpler than superposing vortices with plane waves. However, any spatial dispersion present in the vortex tends to wash out the triangular diffraction pattern. Mourka *et al.* also explored the non-integer case by using a second SLM to mimic the triangular aperture, and further demonstrated that the triangular aperture technique could be applied to SC sources, with a prism correcting for the spatial chirp induced by the forked grating [24]. In this paper, we present a unique approach for generating ultrabroadband optical vortices using two passes off a single segmented SLM, and measuring their charge using the triangular aperture technique.

2. VORTEX GENERATION

The essential element in generating an optical vortex is the now familiar spiral phase plate. The application of this spiral phase to a coherent beam in the near field results in an optical vortex beam in the far field. The applied phase pattern resembles a spiral staircase, where the phase value

along a given azimuth is constant and rises for increasing values of the azimuthal angle. When the maximum value of the phase is equal to an integer multiple of 2π , the resulting far-field intensity pattern is azimuthally symmetric in amplitude with a null at its center [1]. For such a beam, the phase ranges in value from zero to $2\pi m$ as determined by the phase applied in the near field, where m is an integer that defines the “charge” of the vortex. The resulting focal pattern is often referred to as a “donut mode”, and for $m = 1$ is the equivalent of the LG_0^1 (Laguerre-Gaussian) transverse mode.

Since it is common practice to use a SLM to imprint these phase patterns onto an incident beam, the phase distribution is typically written modulo 2π , allowing for the full use of the dynamic range of the SLM in the zero to 2π range, while still allowing for the equivalent of arbitrarily high phases to be expressed [25–27]. A modulo 2π spiral phase pattern of charge m will be made up of m phase segments, each ranging in phase from 0 – 2π . While such a spiral “pinwheel” phase pattern should in principle produce a clean vortex beam, in practice it is usually necessary to spatially separate the properly phase-shifted portions of the incident beam from an unshifted background. For example, in the case of a reflective SLM, a fraction of the beam reflects off of the protective window and other interfaces. For wavelengths that are outside of the anti-reflective coating of the device, this reflection can be especially significant and detrimental. A common approach is to add a “diffraction grating” to the SLM vortex pattern. By applying a tilted phase front to the beam, the phase-shifted portion of the beam is diverted to one side, resulting in the necessary spatial separation from the unshifted part of the beam that remains centered. When displayed modulo 2π , the phase tilt resembles a blazed diffraction grating. In Fig. 1, the spiral phase plate and phase tilt are combined, resulting in the familiar “forked” phase pattern typically used to create optical vortices.

3. SPATIAL CHIRP CORRECTION

When using a broadband source, consideration must be given to the application of a phase pattern over a wide spectral range. Since the SLM phase will be calibrated only for a single color, it may seem that at other wavelengths a proper vortex will not be formed. But due to the application of the blazed grating pattern, only the properly converted “donut” portion of the beam will be diffracted away from the zeroth order. Indeed, the addition of a miscalibrated grating to an equally miscalibrated spiral phase results in an excellent vortex beam for all colors [11,13,14]. Although the vortex for any particular color is intact, there is a spatial separation of different colors in the case of a single forked grating. This is most readily compensated for with a second grating, which removes the spatial chirp [5,28,29]. The technique presented here makes use of a second pass off of a grating imprinted on a portion of our large-aperture SLM. This approach allows for full dynamic control of the spatial chirp compensation independent from the generation of the vortex beams themselves.

To demonstrate theoretically that our double pass configuration generates a broadband vortex beam free of spatial chirp, we unfold our actual setup (to be discussed in a later section) into the straight-line, 6f optical setup shown in Fig. 2.

In this setup, three lenses are placed one focal length apart from each focal plane. A standard grating G is in the front focal plane of lens L1 and a fork grating FG is in the focal plane between lenses L2 and L3. We assume that an initially collimated, ultrashort Gaussian beam approaches the system from the left. We will follow the propagation of each spectral component of the beam separately. We write the spatial amplitude profile of any of the spectral components of the incident field as

$$u_0(x, y) \propto \exp\left\{-\frac{x^2 + y^2}{w_0^2}\right\}, \quad (1)$$

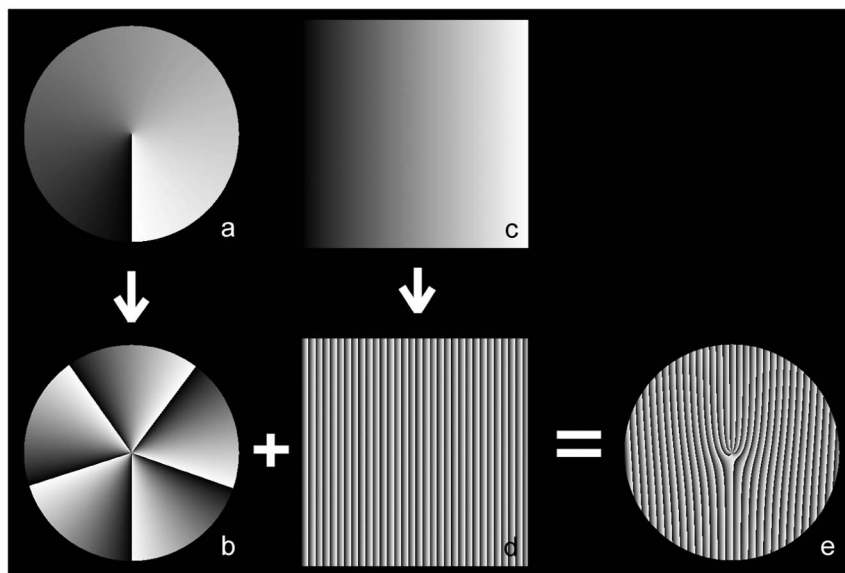


Fig. 1. Spiral phase combined with a phase tilt results in the familiar forked phase pattern. (a) A spiral phase ranging from 0 – 10π is (b) displayed modulo 2π , resulting in a phase plate with five 0 – 2π segments. Likewise, (c) a phase tilt is (d) displayed modulo 2π , resulting in a blazed grating. The addition of these two patterns results in (e) a forked phase pattern.

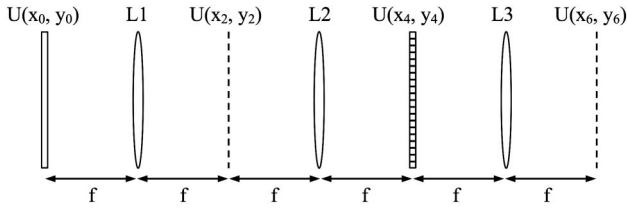


Fig. 2. Unfolded, $6f$ optical system used for spatial chirp correction. From left to right, the field amplitude at each plane is indicated by $U(x, y)$. A grating is placed at plane 0 (the x_0, y_0 plane, which is the first reflection from the SLM), nothing is placed at plane 2 (reflection from our mirror), and a forked grating is placed at plane 4 (second pass off the SLM). The outgoing field is at plane 6. Lenses L1–L3 are all identical.

where w_0 is the beam waist. The incident light beam goes through grating G , and the transmitted light, immediately behind the grating is

$$u_G(x_0, y_0) \propto \exp\left\{-\frac{x_0^2 + y_0^2}{w_0^2}\right\} \exp\left\{in\frac{2\pi}{d}x_0\right\}, \quad (2)$$

where d is the period of the grating, and n is the diffraction order. Because the diffraction angle of the grating is wavelength dependent, the spectral components of the beam will be spatially separated at the $2f$ focal plane. To see this, we evaluate the electric field at the $2f$ Fourier plane by solving the Kirchhoff-Fresnel integral

$$u_{2f}(x_2, y_2) \propto \int_{-\infty}^{\infty} \int_{-\infty}^{\infty} \exp\left\{-\frac{x_0^2 + y_0^2}{w_0^2}\right\} \exp\left\{in\frac{2\pi}{d}x_0\right\} \times \exp\left\{-\frac{ik}{f}(x_0x_2 + y_0y_2)\right\} dx_0 dy_0. \quad (3)$$

By placing an aperture at the $2f$ plane, we allow only the $n = +1$ diffraction order to propagate, such that the resulting light field after the aperture is

$$u_a(x_2, y_2) \propto \exp\left\{-\frac{(x_2 - \lambda f/d)^2 + y_2^2}{(\lambda f/\pi w_0)^2}\right\}. \quad (4)$$

The center of the Gaussian envelope has been laterally displaced by an amount proportional to the wavelength of the spectral component: $x = \lambda f/d$. This field is transmitted through lens L2 to impinge onto the fork grating FG at the $4f$ plane. At this point, the field is

$$u_{4f}(x_4, y_4) \propto \int_{-\infty}^{+\infty} \int_{-\infty}^{+\infty} \exp\left\{-\frac{(x_2 - \lambda f/d)^2 + y_2^2}{(\lambda f/\pi w_0)^2}\right\} \times \exp\left\{\frac{ik}{f}(x_2x_4 + y_2y_4)\right\} dx_2 dy_2. \quad (5)$$

Integrating the above expression gives the electric field just before the fork grating,

$$u_{4f}(x_4, y_4) \propto \exp\left\{-\frac{x_4^2 + y_4^2}{w_0^2}\right\} \exp\left\{i\frac{2\pi}{d}x_4\right\}. \quad (6)$$

The FG adds two phase terms to the light field: one corresponding to a standard diffraction grating and another

corresponding to the vortex charge m . The transmitted light field, immediately behind the FG, is then

$$u_{FG}(x_4, y_4) \propto \exp\left\{-\frac{x_4^2 + y_4^2}{w_0^2}\right\} \exp[-im \tan^{-1}(y_4/x_4)] \times \exp\left\{i\frac{2\pi}{d}x_4(1+N)\right\}, \quad (7)$$

where N is the diffraction order induced by the fork grating. In polar coordinates,

$$u_{FG}(r_4, \varphi_4) \propto \exp\left\{-\frac{r_4^2}{w_0^2}\right\} \exp\{-im\varphi_4\} \times \exp\left[i\frac{2\pi}{d}(1+N)r_4 \cos \varphi_4\right]. \quad (8)$$

Substituting the above result into the Fresnel diffraction integral, we find the vortex field in the final $6f$ Fourier plane to be

$$E(r_6, \varphi_6) \propto \frac{(p-q)^2 w_0^2 \pi^{3/2}}{4} (-i)^m \exp\left\{-\frac{(p-q)^2 w_0^2}{8}\right\} \times \left[Y_{\frac{m-1}{2}}\left(\frac{(p-q)^2 w_0^2}{8}\right) - Y_{\frac{m+1}{2}}\left(\frac{(p-q)^2 w_0^2}{8}\right) \right], \quad (9)$$

where $q = 2\pi(1+N)/d$ and $p = kr_6/f$. The term $Y_\alpha(x)$ is a Bessel function of the second kind. The graphical representation of Eq. (9) is shown in Fig. 3, where we plot cross sectional

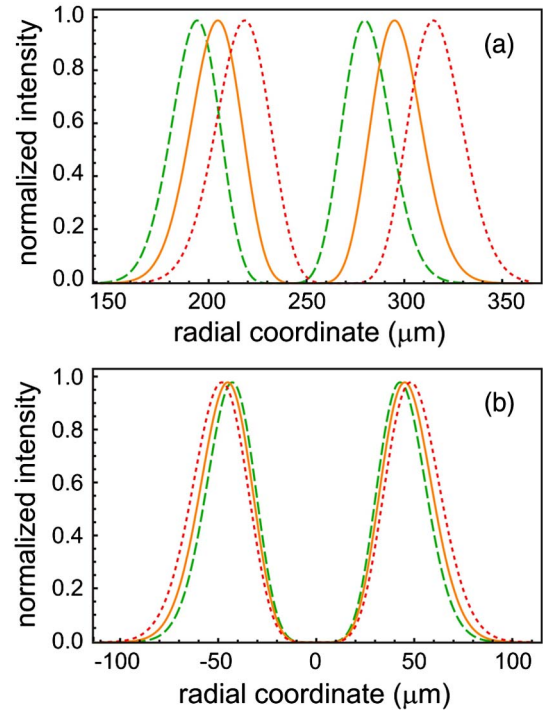


Fig. 3. (Color online) Calculated cross sections of optical vortices (charge $m = 3$) emerging from the (a) doubly chirped and (b) zero-chirp optical system. The three vortices shown in both cases correspond to the wavelengths 550 nm (dashed green line), 580 nm (solid orange line), and 619 nm (dotted red line). For the calculations, we used $f = 70$ cm, $w_0 = 173$ μm , and grating period $d = 325$ μm . These parameters were chosen to approximate the conditions of our experiment.

slices of the electric field intensity. Two solutions for the vortices at this final Fourier plane are of interest. In one solution, the $N = +1$ ($q \neq 0$) diffraction order, the vortices are doubly dispersive, which is shown in Fig. 3(a). The separation of colors is clearly visible, with the red wavelengths getting pushed farther away from the origin compared to the green wavelengths. The other solution corresponds to $N = -1$ ($q = 0$), for which the spatial chirp is eliminated, thus allowing the multiple wavelengths of the broadband light to overlap and form one vortex. This is shown in Fig. 3(b), where we see that the various colors now overlap. We should point out that there is a slight change in the size of the vortex for different wavelengths, as expected and as seen in the figure, but the vortices are now all centered about the origin.

4. TRIANGULAR APERTURE TECHNIQUE

In order to measure the charge of the vortex beams, we employ the triangular diffraction method developed by Hickmann *et al.* [22]. As these authors showed, when an optical vortex illuminates an equilateral triangular aperture, a truncated triangular lattice is produced in the far field that is correlated with the topological charge m of the vortex beam. The triangular lattice results from the superposition of the diffraction patterns from each edge of the triangular aperture. As shown in [22], if a vortex field $\exp(im\phi)$ illuminates the aperture, the far field resulting from diffraction by the horizontal edge (lying along the x transverse Cartesian coordinate) of the aperture is

$$E(k_x, k_y) \propto \delta(k_x - 2\sqrt{3}m/a), \quad (10)$$

where a is the size of each side of the triangle; $k_{x,y}$ are the coordinates in the Fourier plane; and δ is the Dirac delta function. In deriving Eq. (10), the horizontal edge of the aperture was approximated by an infinitesimally wide and infinitely long slit [22]. Equation (10) shows that the diffraction pattern is shifted in reciprocal space by an amount that is proportional to the topological charge m of the vortex beam. The shift for positive m will be in the opposite direction of the shift for negative m . A similar result is obtained for the two slant edges of the aperture. Basically, each aperture edge sends out a light fan in a direction perpendicular to its spatial orientation. For a $m = 0$ field, appreciable interference between the three light fans occurs only at the center of the triangular aperture, creating there a single bright spot. For an incident electric field with $m \neq 0$, the light fans overlap at positions other than the aperture's center. Since diffraction from the edges of a finite sized aperture will also produce parallel and equally spaced satellite fans [30], superposition of the many light fans will create a triangular lattice of bright spots in the Fourier plane whenever $m \neq 0$. The topological charge of the vortex beam determines the size of the triangular lattice since the charge is related to how far the light fans from each edge is shifted in reciprocal space. The diffraction pattern can be used to determine the charge of the beam just by counting the number N of external spots of the resulting triangular lattice. The topological charge is simply $m = N - 1$ [22]. Furthermore, the sign of the charge can also be identified from the orientation of the triangular lattice, which differs by a 180° rotation between positive and negative charges.

This approach has already found success in uncovering the charge of fs vortex beams [23]. In the study present therein, the authors used numerical modeling techniques to theoretically predict the spatial patterns arising from diffraction of cw and fs vortex beams. The modeling indicated that with spatial chirp, the diffraction pattern is quickly washed out with increasing charge or spectral bandwidth. The study also pointed out, however, that if a broadband beam has no spatial chirp, the triangular method is perfectly suited for measuring the charge of ultra-broadband vortex beams. In the work presented here, we combine double-pass spatial chirp compensation with the triangular aperture technique to make broadband vortex charge measurements.

5. EXPERIMENTAL SETUP

A. Laser System

The laser system used for this experiment is a home-built Ti:Sapphire fs oscillator pumped by a Spectra-Physics Millennia at 3 watts. The oscillator emits 50 fs pulses at an 80 MHz repetition rate with an average power of 150 mW. This beam has a center wavelength of roughly 800 nm. After exiting the oscillator cavity, the beam passes through a $4f$ grating pair pulse shaper used for spectral dispersion compensation. After the pulse shaper, the laser (75 mW) is coupled into a microstructured fiber (NKT Femtowhite 800) with a $20\times$ microscope objective. This creates a SC beam with a spectrum that spans from 500 nm to over $1.1 \mu\text{m}$. The output from the SC generator then enters our SLM setup, shown in Fig. 4. The rapidly diverging output from the fiber is collimated with an $f = 70$ cm achromatic lens, and then impinges onto our reflective SLM.

This approach is advantageous since the small core of the fiber ($\sim 1 \mu\text{m}$) acts as an excellent point source. Combined with the relatively long focal length lens (70 cm), a very good plane wave is produced at the face of the SLM. This was confirmed by evaluating the collimated beam with a shear plate near the position of the SLM. Although this approach does not collect all the light from the fiber (the beam expands well beyond the $2''$ diameter of the lens), we have sufficient overhead optical power that this is not a major hindrance.

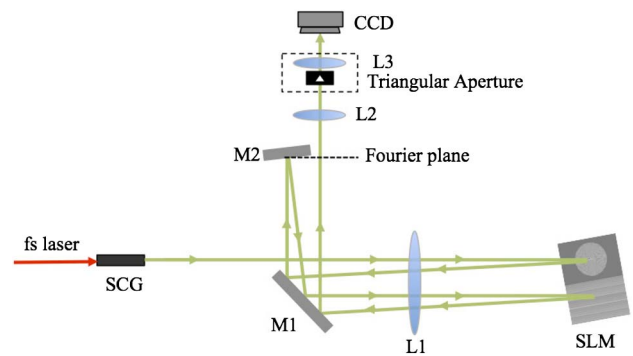


Fig. 4. (Color online) Experimental apparatus for generation of dispersion-free supercontinuum vortices. The items in the dashed box (triangular aperture directly in front of lens) are added to measure the topological charge. SCG, supercontinuum generator; M1, M2, mirrors; L1, 70 cm focal length achromatic lens, $2''$ diameter; L2 = 10 cm and L3 = 15 cm, focal lengths, $1''$ diameter; SLM, spatial light modulator. Beam path is approximate, as beams are large, filling each half of the SLM. Path lengths are as follows: SCG to L1 = 70 cm, L1 to SLM = 70 cm, L1 to Fourier plane = 70 cm, Fourier plane to L2 ~ 20 cm, L2 to L3 ~ 20 cm, L3 to CCD = 15 cm.

Note that in the results presented here, cw, fs, and SC, all of the optical paths are similar. All beams are coming from the SC fiber source, and it is simply the laser operation and power that are adjusted. To adjust the laser parameters to explore the three different cases of cw, fs, or SC, the following prescription is used. For cw, the laser is put in cw mode (<4 nm bandwidth). This beam enters and exits the fiber as a cw beam. For fs, the laser is modelocked, but an attenuator is used before the fiber to keep the power low. Thus there is no SC generation in the fiber, and the input 40 nm bandwidth exits the fiber as a 40 nm bandwidth. For the SC studies, the attenuator is removed, allowing for enough power to enter the fiber and to create the SC. This spectrum is broad, ranging from the green (~ 550 nm) to the near-infrared (~ 1.2 μm).

B. Zero Spatial Chirp

As shown in Fig. 4, the return beam from the first half of the SLM travels back through the 70 cm lens, where it is steered with mirror M1 onto a second mirror M2. Mirror M2 is situated 70 cm from the lens, in the image plane of the $4f$ system. With a blazed forked grating on the first half of the SLM, three spots appear in the image plane: the $+1$, 0 , and -1 diffracted orders. Because of the encoded blaze in the phase pattern, most of the optical power appears as a vortex in the $+1$ diffracted order. The 0 and -1 orders can be blocked by a razor blade. Mirror M2 then directs the $+1$ order back through the lens, toward the second half of the SLM, which contains a blazed diffraction grating (identical to the first, simply without the vortex). The beam again travels back through the lens at a slightly different angle, skimming past mirror M2 on its way to a 10 cm lens, which is used to image the vortex onto the CCD camera (Dataray Windcam-D). All three diffracted orders ($+1$, 0 , -1) may be viewed simultaneously on the camera, or a razor blade may be inserted in the Fourier plane to isolate certain orders (in an effort to improve visibility on the camera).

C. Triangular Aperture

The experimental results presented here consist of two distinct elements. The first is the production of vortices with no spatial dispersion. This was achieved with the setup shown in Fig. 4, and the results are presented in the next section. The second step consisted of measuring the topological charge of these vortices using the triangular aperture technique. To do this, the lens L2 was adjusted to magnify the focused vortex beam to the approximate size of our triangular apertures, shown in the dashed box in Fig. 4. Triangular apertures of different sizes were made by adhering metallic adhesive tape to a substrate with large holes in it, thus providing an aperture in air [23]. The entire housing was mounted on an x - y translation stage in order to carefully align the triangular aperture with the vortex beam. A 15 cm lens (L3) was placed immediately after the triangular aperture in order to image the diffraction pattern onto the CCD array. Images were recorded on a monochrome CCD array (Dataray WinCam-D) or a color CCD array (Canon T2).

D. Spatial Light Modulator

The SLM (Hamamatsu X8267-14) is a back-illuminated liquid-crystal-on-silicon design that eliminates pixilation and has a 100% fill factor. The reflective nature of this device is ideal for high power beams (it can handle an amplified system

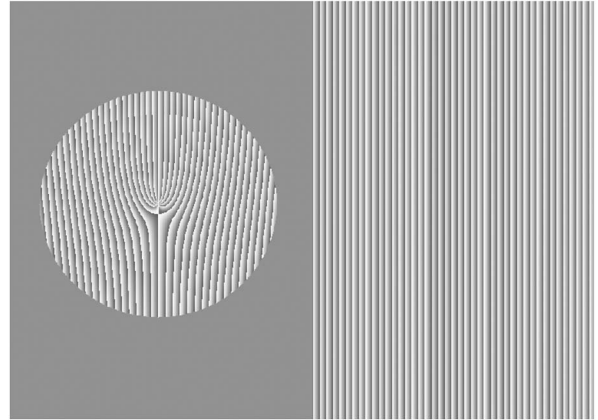


Fig. 5. Screenshot of the grayscale pattern displayed on the SLM. The left half of the SLM displays an apodized forked grating for generating a vortex beam. The right half displays only a blazed grating.

as well). Our particular device is antireflection (AR) coated for 800 nm, which means that it is difficult to efficiently diffract energy at visible wavelengths. But if there is sufficient power at shorter wavelengths, this problem may be compensated for with a proper choice of grayscale settings to achieve a user-designed color balance more representative of visual “white” [31]. The SLM acts as a phase-only filter, with the grayscale level indicating the level of added phase (black = 0, white = 2π). This is a well-known technique for beam modulation. A LabView program was written to control the SLM. Since this is a large aperture SLM (2 cm \times 2 cm), there is ample room to segment the active area. A screenshot of the pattern applied to the SLM is shown in Fig. 5. In this figure, the two independent halves of the SLM are clearly seen: the left half of the SLM contains a forked grating inside a circular apodizing function (giving better vortex beams), the right side of the SLM contains a blazed grating. Note that the grating spacing is identical on each half of the SLM. This arrangement has several advantages. First, it is completely programmable, meaning either section may be turned off for direct comparison to the single pass case. Second, the blaze angle may be reversed on the second pass, leading to a doubly dispersive element. Third, the grayscale levels may be adjusted to maximize the diffraction efficiency at a particular wavelength. And fourth, the ability to rapidly change the phase patterns means that “optimum” solutions could be found in a feedback arrangement [32].

6. RESULTS

A. Zero Spatial Chirp

Using this experimental arrangement, we have observed that with a single pass off of a forked grating, high-quality broadband vortices are produced by the SC fiber source, albeit with spatial chirp. With the new alignment scheme presented here (i.e., sending the beam back for a second pass off the SLM), this so-called double-pass configuration allows us to make the system either doubly dispersive, or corrected (spatial chirp removed). Namely, we can add even more spatial chirp to the beam (doubly dispersive), by using the $+1$ diffracted order on the first pass, and the -1 order on the second pass. To remove the spatial chirp entirely (corrected case), the $+1$ diffracted orders are used on each pass (note the orientation is reversed because of the reflection from the mirror). The

unique advantage of a fully programmable system, as opposed to a static holographic plate, is it allows the user to generate extra spatial chirp, or to remove it altogether. In all the results presented herein, we have chosen to compare the dispersion-corrected case to the doubly dispersive case, rather than to the single forked grating case. This is both illustrative (the single-forked grating generates roughly half the spatial chirp) and demonstrative (the unique versatility of this approach allows for precise tailoring of spatial chirp, which could be useful in various pulse measurement schemes, for example [33].)

By switching the grating blaze angle on the second pass, we can switch between the doubly dispersive and the dispersion-corrected case. In order to explore the effect this has on laser bandwidth, we observe three separate laser modes (cw, fs, and SC) by adjusting the modelocking and laser power as explained in the experimental section earlier. (Note that the optical geometry shown in Fig. 4 is identical for all three laser modes.) Figure 6 shows the results, where the top row shows a charge 3 cw vortex generated in the doubly dispersive case (left) and the corrected case (right). As expected, there is little difference for the doubly dispersive or corrected configurations with a cw beam. (Note that the energy distribution in all the vortices presented here is not perfectly uniform due to small distortions in our optical system.) The second row shows the same experiment, but this time with a fs pulse of approximately 40 nm bandwidth. There is clearly spatial dispersion in the left pane, and the spatial dispersion is removed in the right pane. In the third row of Fig. 6, the full SC beam is used. The amount of bandwidth recorded here is large (~ 120 nm) compared to the fs case, effectively destroying our doubly dispersed vortex, i.e., there is no remaining singularity (hole) in the beam, as seen in Fig. 6(c). By including the second grating in our double-pass configuration, the spatial dispersion is corrected, effectively restoring the vortex, as seen in Fig. 6(f). In fact, the three vortices presented in the right column look remarkably similar, despite the dramatic increase in bandwidth.

The SC fiber source has a spectrum that spans from 500 nm to over 1100 nm. The image recorded here, however, has a much narrower spectral bandwidth for two reasons. First, the SLM is broadband AR coated, which means it is

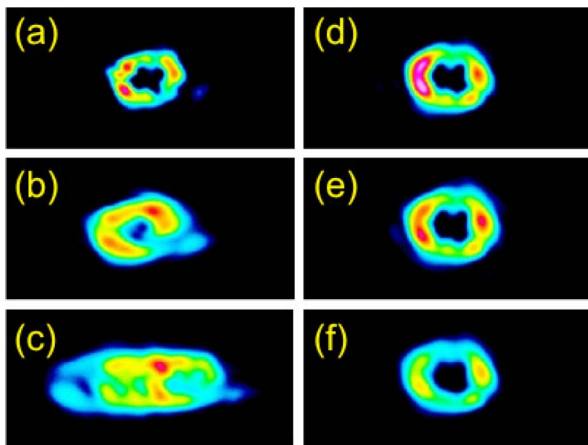


Fig. 6. (Color online) Charge 3 vortex is generated in the doubly dispersive case for (a) continuous wave (CW), (b) femtosecond (fs), and (c) supercontinuum (NIR SC). The dispersion-corrected case is shown for (d) CW, (e) fs, and (f) NIR SC.

rather lossy at wavelengths far from the design wavelength of 800 nm. Second, the silicon CCD array has higher response in the 800–900 nm range than at shorter or longer wavelengths.

In an effort to visualize this result for the full spectrum of the SC, the monochrome CCD array was replaced by a color CCD array. In this case, we used a digital single lens reflex camera (Canon T2), and removed the camera's lens in order to image directly onto the CCD array. These cameras consist of a standard monochrome CCD array with an RGB filter on top of the array. The RGB filter is segmented to give rows of red, green, and blue, thus reproducing a true color image. The results are shown in Fig. 7. The first row shows a vortex at a center wavelength of 550 nm. This was achieved by using a variable wavelength filter at the output of the fiber. By adjusting the position of this filter transverse to the beam, different spectral regions of a bandwidth equal to 10 nm are allowed to pass through. The left column of Fig. 7 shows the doubly dispersive results, and the right column shows the corrected results. Note that the position of the vortices in the left column shift horizontally as the wavelength is increased from 550 nm to 580 nm to 619 nm due to grating diffraction. The right column shows the corrected results, and it is clear that there is no lateral shift of the beam in this case; the spatial dispersion has

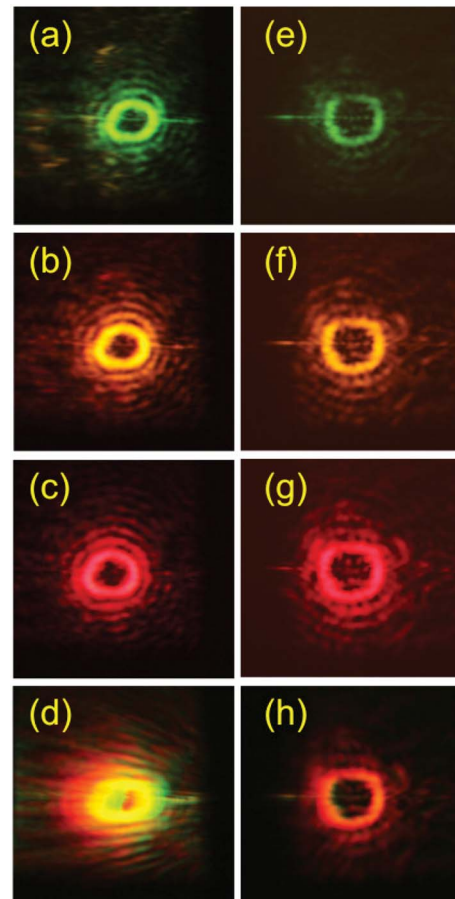


Fig. 7. (Color online) Color vortices are recorded with a color DSLR CCD array. The left column shows the doubly dispersive results at wavelengths (a) 550 nm, (b) 580 nm, (c) 619 nm, and (d) full spectrum. The right column shows the dispersion-corrected results for (e) 550 nm, (f) 580 nm, (g) 619 nm, and (h) full spectrum.

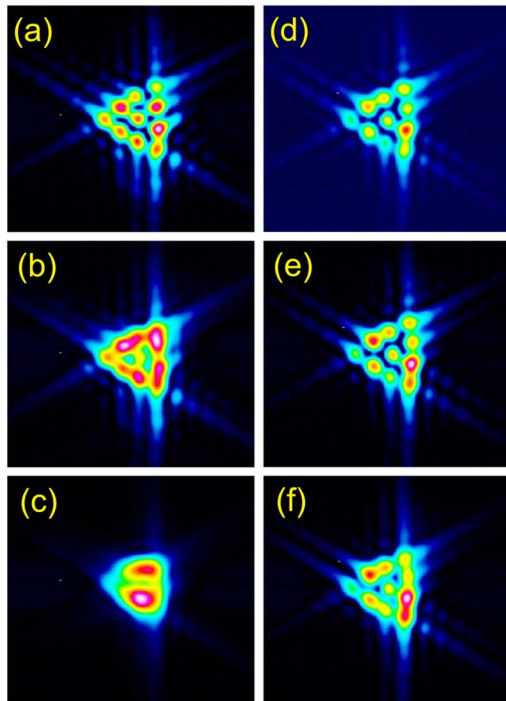


Fig. 8. (Color online) False-color diffraction patterns in the near infrared from a 0.73 mm triangular aperture of charge 3 vortices. The left column shows the doubly dispersive case for (a) cw, (b) femtosecond, and (c) supercontinuum modes. The right column shows the dispersion-corrected case for (d) cw, (e) femtosecond, and (f) supercontinuum modes.

been corrected. The bottom row shows the full spectrum from the SC source, both in the doubly dispersive case (left) and the corrected case (right).

As seen in the bottom row of Fig. 7, there is a dramatic improvement in the spatial quality of the vortex beam for the doubly dispersive and corrected case when using ultra-broadband sources. The residual red tint is simply a response of the diffraction efficiency of our device, which favors red light. After a second pass off the SLM, the amount of green light diminishes rapidly. However, this could, in principle, be compensated for with an appropriate weighting of the input spectrum and a change to the grayscale of the SLM, making it possible to obtain a better color balance in the final vortex.

B. Triangular Aperture

In Fig. 8(a) we show the vortex diffraction pattern from a triangular aperture seen when the laser, operating in cw mode, makes a doubly dispersive pass through the system. A lattice of spots arranged in a triangular pattern is formed. The number of spots along the side of the outer triangle is one greater than the vortex's topological charge [22]. In this particular case, four spots can be counted, corresponding to a charge 3 vortex. In fs mode, Fig. 8(b), the triangular pattern is still discernible, although the spots are smeared. This smearing was attributed to the spatial chirp suffered by the broadband vortex, and numerical simulations supported this hypothesis [23]. For higher charge vortices, smearing of the individual spots near the edges of the pattern makes it impossible to count the number of spots, limiting the applicability of the technique [23]. When a SC spectrum is being generated in

the fiber, the spots are severely smeared, and a triangular lattice can no longer be identified, as seen in Fig. 8(c).

Correcting the spatial chirp greatly improves the triangular aperture technique when using a broadband source. In Fig. 8(d), we see that, as is expected, the cw diffraction pattern is unchanged when using the dispersion correction. However, in fs mode, a significant improvement occurs, as seen in Fig. 8(e). The diffraction pattern is as clearly defined as in the cw case, with no smearing of the spots. With spatial chirp corrected, the technique works well even in the SC case, as shown in Figure 8(f). Although not as sharply defined as in the cw and fs modes of operation, the resulting triangular lattice is clearly discernible and one can easily

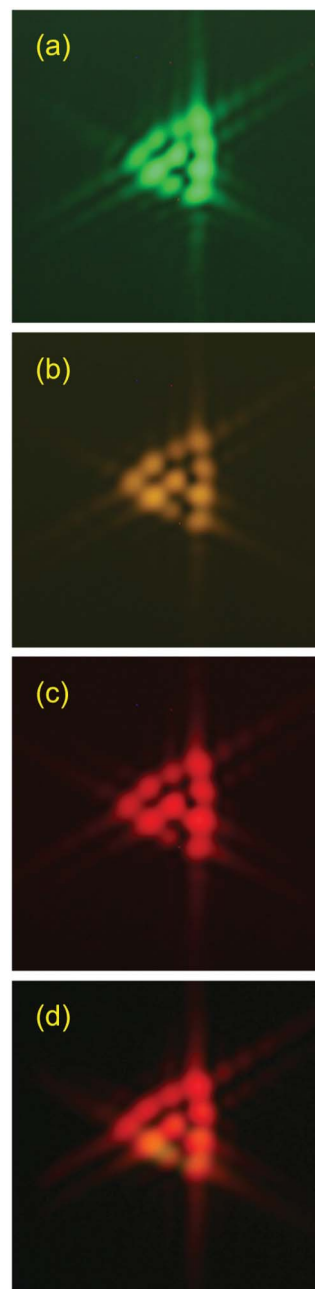


Fig. 9. (Color online) True-color diffraction patterns in the visible for a charge 3 supercontinuum vortex from a 0.73 mm triangular aperture: (a) 523 nm, (b) 580 nm, (c) 620 nm, and (d) full spectrum.

count the number of spots in the lattice to determine the vortex charge.

When using the color CCD camera and the variable bandpass filter, we see a similar triangular lattice generated by the SC vortex in the visible spectrum, as shown in Figs. 9(a)–9(c). The last panel, Fig. 9(d), shows the full SC spectrum, obtained by removing the filter entirely. In each case, the topological charge is easily ascertained from the diffraction pattern. This triangular aperture technique is a simple and quick tool to spectrally resolve the topological structure of SC vortices. These images show that the topological charge of the SC vortex is uniform across its spectrum in that all images are consistent with a charge three vortex.

It is interesting to note that both the technique presented here and the method of Denisenko *et al.* [20] make use of the intensity profile in the far field to determine the topological charge of polychromatic vortices. Here, a triangular aperture is used to generate a pattern of spots, while in the previous work a cylindrical lens is used to generate a pattern of dark stripes. In the work presented here, a second pass off of the SLM is used to compensate for smearing due to spatial chirp, while Denisenko *et al.* use a variable filter to image narrow spectral regions individually [20]. Clearly, both techniques are useful to measure topological charge, and it certainly would not be surprising if other lens or aperture geometries would yield similar results.

7. CONCLUSION

We have presented results on generating ultra-broadband vortex beams, and correcting the spatial dispersion problems that plague vortex beams made with a single forked grating. This approach relies on the use of a single SLM segmented into two parts, with each part being independently programmable. The use of a single SLM greatly alleviates the complexity of two grating setups, is more economical, and improves the overall optical stability of the setup.

We also studied the diffraction of vortex beams on a triangular aperture as a tool for determining the vortices' topological charge. We compared the cases of cw and pulsed (fs and SC) vortices. When an ultrabroadband vortex beam is generated via a forked grating, the grating introduces spatial dispersion of the various color components of the vortex that can significantly smear the diffraction pattern. We found that while the triangular aperture technique can still be used with fs pulses, it is useless for SC vortices due to the extreme spatial dispersion of the broadband source. However, we showed that if the spatial dispersion is compensated, the technique works well with cw and pulsed vortex beams, even in the SC case. Using color filters to spectrally resolve the diffraction pattern, the topological structure of ultrabroadband vortices can be studied with the triangular-aperture technique across a range of colors. In our particular case, the topological charge of the SC vortex was uniform across its whole spectrum, but the technique could be useful in characterizing vortex beams having more complex topological structures.

ACKNOWLEDGMENTS

Luís E. E. de Araujo thanks Fundação de Amparo à Pesquisa do Estado de São Paulo for financial assistance. Matthew

Anderson would like to acknowledge financial support from the San Diego Foundation Blasker Grant.

REFERENCES

1. J. F. Nye and M. V. Berry, "Dislocations in wave trains," *Proc. R. Soc. A* **336**, 165–190 (1974).
2. L. Allen, M. W. Beijersbergen, R. J. C. Spreeuw, and J. P. Woerdman, "Orbital angular momentum of light and the transformation of Laguerre-Gaussian laser modes," *Phys. Rev. A* **45**, 8185–8189 (1992).
3. M. R. Dennis, K. O'Holleran, and M. J. Padgett, "Singular optics: optical vortices and polarization singularities," in *Progress in Optics* (Elsevier, 2009), Vol. **53**, pp. 293–363.
4. L. Allen and M. Padgett, "The orbital angular momentum of light: An introduction," in *Twisted Photons: Applications of Light with Orbital Angular Momentum* 1st ed., J. P. Torres and L. Torner, eds. (Wiley-VCH, 2011).
5. K. Bezuhanov, A. Dreischuh, G. G. Paulus, M. G. Schätzel, and H. Walther, "Vortices in femtosecond laser fields," *Opt. Lett.* **29**, 1942–1944 (2004).
6. I. G. Mariyenko, J. Strohaber, and C. J. G. J. Uiterwaal, "Creation of optical vortices in femtosecond pulses," *Opt. Express* **13**, 7599–7608 (2005).
7. K. Bezuhanov, A. Dreischuh, G. G. Paulus, M. G. Schätzel, H. Walther, D. Neshev, W. Królikowski, and Y. Kivshar, "Spatial phase dislocations in femtosecond laser pulses," *J. Opt. Soc. Am. B* **23**, 26–35 (2006).
8. I. Zeylikovich, H. I. Sztul, V. Kartazaev, T. Le, and R. R. Alfano, "Ultrashort Laguerre-Gaussian pulses with angular and group velocity dispersion compensation," *Opt. Lett.* **32**, 2025–2027 (2007).
9. A. Schwarz and W. Rudolph, "Dispersion-compensating beam shaper for femtosecond optical vortex beams," *Opt. Lett.* **33**, 2970–2972 (2008).
10. Ó. Martínez-Matos, José A. Rodrigo, M. P. Hernández-Garay, J. G. Izquierdo, R. Weigand, M. L. Calvo, P. Cheben, P. Vaveliuk, and L. Bañares, "Generation of femtosecond paraxial beams with arbitrary spatial distribution," *Opt. Lett.* **35**, 652–654 (2010).
11. A. J. Wright, J. M. Girkin, G. M. Gibson, J. Leach, and M. J. Padgett, "Transfer of orbital angular momentum from a supercontinuum, white-light beam," *Opt. Express* **16**, 9495–9500 (2008).
12. M. V. Berry, "Coloured phase singularities," *New J. Phys.* **4**, 66.1–66.14 (2002).
13. J. Leach and M. J. Padgett, "Observation of chromatic effects near a white-light vortex," *New J. Phys.* **5**, 154 (2003).
14. J. Leach, G. M. Gibson, M. J. Padgett, E. Esposito, G. McConnell, A. J. Wright, and J. M. Girkin, "Generation of achromatic Bessel beams using a compensated spatial light modulator," *Opt. Express* **14**, 5581–5587 (2006).
15. Y. Tokizane, K. Oka, and R. Morita, "Supercontinuum optical vortex pulse generation without spatial or topological-charge dispersion," *Opt. Express* **17**, 14517–14525 (2009).
16. I. Moreno, J. A. Davis, B. M. L. Pascoguin, M. J. Mityr, and D. M. Cottrell, "Vortex sensing diffraction gratings," *Opt. Lett.* **34**, 2927–2929 (2009).
17. G. C. G. Berkhout, M. P. J. Lavery, J. Courtial, M. W. Beijersbergen, and M. J. Padgett, "Efficient sorting of orbital angular momentum states of light," *Phys. Rev. Lett.* **105**, 153601 (2010).
18. M. P. J. Lavery, G. C. G. Berkhout, J. Courtial, and M. J. Padgett, "Measurement of the light orbital angular momentum spectrum using an optical geometric transformation," *J. Opt.* **13**, 064006 (2011).
19. X. C. Yuan, N. Zhang, and R. E. Burge, "Extending the detection range of optical vortices by Dammann vortex gratings," *Opt. Lett.* **35**, 3495–3497 (2010).
20. V. Denisenko, V. Shvedov, A. S. Desyatnikov, D. N. Neshev, W. Krolikowski, A. Volyar, M. Soskin, and Y. S. Kivshar, "Determination of topological charges of polychromatic optical vortices," *Opt. Express* **17**, 23374–23379 (2009).
21. V. G. Shvedov, C. Hnatovsky, W. Krolikowski, and A. V. Rode, "Efficient beam converter for the generation of high-power femtosecond vortices," *Opt. Lett.* **35**, 2660–2662 (2010).

22. J. M. Hickmann, E. J. S. Fonseca, W. C. Soares, and S. Chavez-Cerda, "Unveiling a truncated optical lattice associated with a triangular aperture using light's orbital angular momentum," *Phys. Rev. Lett.* **105**, 053904 (2010).
23. L. E. E. de Araujo and M. E. Anderson, "Measuring vortex charge with a triangular aperture," *Opt. Lett.* **36**, 787–789 (2011).
24. A. Mourka, J. Baumgartl, C. Shanor, K. Dholakia, and E. M. Wright, "Visualization of the birth of an optical vortex using diffraction from a triangular aperture," *Opt. Express* **19**, 5760–5771 (2011).
25. M. Reicherter, T. Haist, E. U. Wagemann, and H. J. Tiziani, "Optical particle trapping with computer-generated holograms written on a liquid-crystal display," *Opt. Lett.* **24**, 608–610 (1999).
26. D. Ganic, X-S. Gan, M. Gu, M. Hain, S. Somalingam, S. Stankovic, and T. Tschudi, "Generation of doughnut laser beams by use of a liquid-crystal cell with a conversion efficiency near 100%," *Opt. Lett.* **27**, 1351–1353 (2002).
27. K. Crabtree, J. A. Davis, and I. Moreno, "Optical processing with vortex-producing lenses," *Appl. Opt.* **43**, 1360–1367 (2004).
28. G. F. Brand, "The forked blazed grating as a quasioptical element For gyrotron applications," *Internation. J. Infrared Mill. Waves* **20**, 1207–1219 (1999).
29. A. Ya Bekshaev and A. I. Karamoch, "Spatial characteristics of vortex light beams produced by diffraction gratings with embedded phase singularity," *Opt. Commun.* **281**, 1366–1374 (2008).
30. R. C. Smith and J. S. Marsh, "Diffraction patterns of simple apertures," *J. Opt. Soc. Am.* **64**, 798–803 (1974).
31. J. Albero, I. Moreno, and J. Campos, "Enhancement of the broadband modulation diffraction efficiency of liquid-crystal displays," *Opt. Lett.* **37**, 52–54 (2012).
32. A. Jesacher, A. Schwaighofer, S. Fürhapter, C. Maurer, S. Bernet, and M. Ritsch-Marte, "Wavefront correction of spatial light modulators using an optical vortex image," *Opt. Express* **15**, 5801–5808 (2007).
33. E. M. Kosik, A. Radunsky, I. A. Walmsley, and C. Dorrer, "Interferometric technique for measuring broadband ultrashort pulses at the sampling limit," *Opt. Lett.* **30**, 326–328 (2005).